Encrypted wide-field two-photon microscopy with single-pixel detection and compressed sensing

Yu-Xuan Ren[1,4], Cihang Kong[1,2,4], Hongsen He[1], Xinglin Zeng[1,3], Kevin K. Tsia[1], and Kenneth K.Y. Wong[1]*

[1]*Department of Electrical and Electronic Engineering, The University of Hong Kong, Pokfulam Road, Hong Kong, China*

[2]*Department of Physics, University of Bielefeld, Universitätsstraße, 25, 33615 Bielefeld, Germany*

[3]*Max-Planck Institute for the Science of Light, Staudtstraße 2, 91058 Erlangen, Germany.*

[4]*Equal contribution*

*E-mail: kywong@eee.hku.hk

We demonstrate a single-pixel two-photon microscopy using a compact femtosecond fiber laser by spatially tailoring the beam into orthogonal basis for patterned illumination. Such wide-field illumination excites a weak two-photon fluorescence signal that can be detected by a photomultiplier tube (PMT). An encrypted hybrid basis with random element sequence of Hadamard basis is adopted to illuminate the sample. The hybrid basis shares the same differential detection with Hadamard basis, and greatly reduces the number of measurements compared with random basis. The reduced number of measurements was demonstrated by using compressed sensing, which allows the minimum image collection and transfer bandwidth.

The advanced array sensor technology, such as charge coupled devices (CCD) and complementary metal oxide semiconductor (CMOS), has revolutionized the image recording and storage [1]. Nevertheless, the array sensor encounters bottlenecks such as compromised sensitivity and restricted readout speed. In contrast, single-pixel imaging takes advantage of spatially or temporally structured illumination to reconstruct the spatial or temporal object [2,3], minimizes the use of array detector, and alleviates the requirement of storage. The single-pixel detection was able to resolve images within broad spectrum spanning from X-ray, visible, infrared, to terahertz [4-9], with the ability to image objects under both the bright-field and fluorescence modules [10,11]. The single pixel detection has shown its potential in multimodal microscopy including, color, gray-scale, diffractive, phase, amplitude, and in general, complex field [10-16]. Two-photon excitation is a nonlinear process, which requires a pair of photons to reach a single fluorophore molecule within a considerably narrow temporal interval [17]. The fluorescence intensity is proportional to the square of the excitation intensity, therefore, the two-photon microscopy (TPM) provides an effective excitation/detection method at a deep position within scattering samples [18]. The TPM can be achieved by focusing an ultrashort pulsed laser into a diffraction-limited spot and mapping the signal using a point-by-point scanning [19]. The power density for the focused femtosecond laser is sufficient to excite the two-photon fluorescence with an average laser power of a few mW (power density of $\sim 10 mW/\mu m^2$) [19-21]. Although the single-pixel TPM with modulated light illumination has been demonstrated using a line focused beam with an orthogonal spatially modulated basis along one dimension [22], however, the wide-field TPM is still challenging preferentially due to the spreading of the beam over the whole field of view and the greatly reduced power density.

We hereby demonstrate a single-pixel TPM using a custom-built mode-locked fiber laser, operating at 1019 nm wavelength and 80 MHz repetition rate. Further, we employ photomultiplier tube (PMT) as the bucket detector to register the integral fluorescence counts. In addition, we augmented the performance of the single pixel camera with a hybrid basis combining the Hadamard matrix and random sequence encryption. The fiber laser employed a 25-cm highly ytterbium-doped fiber (YDF, Thorlabs Yb 1200-4/125) as gain medium pumped by a diode laser (II-VI, LC96Z600, 600 mW) operating at 976 nm (Fig. 1). The pump beam (laser output) were coupled into (out of) the fiber cavity in reflection mode via an optical integrated module (OIM), which integrates the wavelength-division multiplexing (WDM), polarization-sensitive isolation (PS-ISO) and 50:50 beam splitting (BS). The mode-locked pulsed laser, operated in the all-normal dispersion regime, self-starts from initial

noise via nonlinear polarization rotation [23]. The mode-locking was stabilized by a bandpass filter (BPF, Semrock, LL01-1064-12.5, FWHM 4 nm) placed between two fiber collimators (Col). In contradistinction to spectral tuning [24], control of the minute tilt angle of the BPF allows fine tuning of the central wavelength. The polarization state was flexibly manipulated by a half-wave plate (λ/2) and an inline polarization controller (PC). The self-started operation was achieved by tuning the intra-cavity PC and waveplates [23,25]. Direct output (12 mW) from the cavity was amplified by chirped pulse amplification (CPA) [26]. In brief, the laser was chirped through a 50-m SMF (HI 1060, Corning) to about 25 ps. The power was boosted up by cascaded highly doped YDFs (Yb 1200-4/125, Thorlabs) [21]. The pulses were further de-chirped by a compressing unit using a pair of polarization insensitive gratings (LightSmyth, T-1000-1040-3212-94) and a quarter waveplate. The amplified laser was released into free space with an output beam diameter of ~4.0 mm through a fiber collimator. The compressed beam has an average power of ~300 mW (pulse energy of 3.75 nJ), and a power stability of ~ 0.5 % over 1 hr (the stability during measurement is better than 0.3%).

The compressed femtosecond laser was spatially expanded by a telescope and tailored by a spatial light modulator (SLM, Holoeye Pluto, 1920x1080). Here, we used a high-NA objective (O1, Nikon, 100x, NA=1.3 Oil immersion) to compromise the collection angle and the field of view. A half-wave plate placed before the PBS adjusts the average power [Fig. 1(b)]. Typically, the average power (pulse energy) was ~60 mW (0.75 nJ). The average (peak) power density for the field of view of $60\ \mu m \times 60 \mu m$ is $16\ \mu W/\mu m^2$ ($379\ \mu W/\mu m^2$). The excited two-photon fluorescence, collected by the same objective, was split off the excitation beam by a dichroic mirror (DM, Semrock, FF776). The two-photon emission was detected by a large-area photomultiplier tube (PMT, Hamamatsu H10723-20) via a tube lens (f=200 mm). Two identical short pass filters (Semrock, BSP01-785R) remove the excitation light. The electrical signal produced by the PMT was registered on the control computer through an analogue-to-digital (A/D) converter (NI-PCI-6110). The signal was sampled at 20 kS/s and averaged over an exposure time of 0.1 s~ 0.4 s. The alignment was assisted by a lower magnification objective (Nikon, 20x, S Plan Fluor, NA=0.45) and a CMOS camera (IDS, UI-1240SE-M), which collects the bright-field image under wide-field illumination.

When the structured patterns, i.e., a series of orthogonal basis ψ_n, excite the two-photon fluorescence, the single-pixel PMT receives a photon count signal (the weighting coefficient) ω_n. The image recovery was performed by the sum over all the measurements,

$x = \sum_{n=1}^{N} \omega_n \psi_n$, where N is the number of measurements, which equals the number of pixels. The projected pattern can be random speckles, spectrum harmonics, or arbitrary patterns, as long as the patterns are mutually orthogonal [2,4,12,27,28]. We explore the Hadamard matrix, which follows the recursion equation, $H_1 = [1]$, $H_{2n} = [H_n, H_n; H_n, -H_n]$, and the entries are either -1 or 1. The rows in Hadamard matrix are mutually orthogonal and the matrix satisfies the equality $H_n H_n^T = nI_n$, where I_n is an identity matrix of dimension n. The conjugate transpose of the Hermitian Hadamard matrix equals itself, i.e., $(H_n^T)^* = H_n$ ('*' denotes the complex conjugate). Fig. 1(c) demonstrates the single pixel detection with structured illumination under bright-field. The bee image is illuminated by a complete set of orthogonal basis ψ_n (specifically Hadamard basis), while the single-pixel detector registers the weighting coefficients ω_n, without any spatial resolution. The right-most image in Fig. 1(c) shows the single-pixel bright-field image with an image pixel resolution of 64x64. In the following, we will extend the Hadamard bases to hybrid bases with randomized element sequence, and such random sequence offers encryption and increased complexity to decipher the original image.

The mode-locked fiber laser was sampled by a 10-GHz high speed photodetector (HP 11982A), and digitalized by a real-time oscilloscope (Lecroy SDA 820Zi-B) operating at 40GS/s. The period (repetition rate) of the mode-locked pulse is 12.5 ns (80 MHz) [Fig. 2 (a)]. The tilting angle of the bandpass filter was tuned with an optical spectrum analyzer (AQ6370D, Yokogawa), which monitors the optical spectrum. Fig. 2(b) presents the measured spectrum (blue) and the Gaussian fitting (red), which suggests a central wavelength of 1019 nm with a FWHM of ~3 nm. The temporal pulse width was evaluated by an optical correlator (Femtochrome Inc, FR-102MN). Both the autocorrelation curve [blue in Fig. 2(c)] and the fitting [red in Fig. 2(c)] show a good Gaussian shape with a FWHM of ~550 fs (Fig. 2).

The spatially expanded ultra-short pulsed laser was further tailored by the SLM projected with structured patterns. We here proposed a hybrid basis incorporating Hadamard basis and the random sequence to excite the two-photon fluorescence. The Hadamard basis, i.e., each row in a large Hadamard matrix of $N^4 \times N^4$, is reshaped into a square matrix of $N \times N$. The hybrid basis was acquired by randomizing the element sequence in Hadamard basis. Since the hybrid basis is also made of 1's and -1's, it can be split into two complementary patterns depending on the sign of the element [Fig. 3(a)]. The proposed hybrid basis offers two advantages, first, it inherits the advantage of minimum detection noise from differential detection. Second, the random sequence ordering of Hadamard basis offers a greatly reduced

number of measurements as compared with the speckle-like incoherent basis. Fig. 3(a) shows how the proposed hybrid basis is formed by randomizing the element sequence of a Hadamard basis. The Hadamard basis was taken from one selected row of the Hadamard matrix, and reshaped into a square. The square pattern is then hybridized by randomizing the element sequence followed by splitting the basis into two complementary patterns according to the element sign. The SLM presents the complementary patterns in sequence, and the measurement with negative basis was subtracted from that with positive basis. The illumination with the pair patterns allows the elimination of the background noise in the weight coefficients, and the improved image quality. In contrast to purely random basis, e.g., the Gaussian noise, the hybrid basis greatly reduces the dimension, and the number of measurements.

Figure 3(b) shows the detected signal for two complementary patterns as well as the differential signal as function of the basis index. Here, the random numbers act as encryption key to secure the image. Image decoding is impossible without knowledge of the random sequence. For example, if the third party wants to decipher the image with only the Hadamard basis, the eavesdropping image will show random speckles [Fig. 3(d)]. The implementation of the wide-field TPM [Fig. 3(c)] has been corroborated by the bright-field microscopy [Fig. 3(e)] using the bright-field illumination and five microspheres with diameter 10 μm as sample. Fig. 3(f~h) show some more images for various microspheres and multiple inter-particle orientations captured with the pseudo-random sequenced Hadamard patterns, which imply an isotropic resolution. The encryption is done simultaneously when the single pixel detection records the image, thus ensures the secure image transfer in subsequent steps. Although similar optical encryption was performed on computational ghost imaging [29,30], the proposed hybrid basis greatly reduces the number of measurements, in addition to the inhibition of noise.

Since the signal for two-photon wide-field image is extremely weak, we sum over a certain period (exposure time) to increase the signal-to-noise ratio. Due to slow refresh rate of the liquid crystal SLM (~60Hz), projection of 8192 (64x64x2) patterns takes over a few minutes. The projection time can be further minimized by using the digital micromirror devices (DMD), which features with fast refresh rate over tens of kilohertz [1,31]. On the other hand, the speed can be improved by compressive sensing that measures reduced sampling points [27,32]. Nyquist theorem states that the sampling rate should be at least twice the highest frequency. However, when the sample information is sparse (most weighting coefficients are small), the compressed sensing can break this limit. Recall that the single-pixel measurement

performs the matrix multiplication $\omega = \psi x$, and the compressed sensing recovers the raw image x (with N pixels) with smaller number of measurements $K \ll N$. In accordance, the ratio K/N is defined as the compressing ratio CR. The compressed sensing minimizes either the $l1$-norm $||x||_1$ or the total variance $TV(x) = \sqrt{(\partial_i x)^2 + \left(\partial_j x\right)^2}$ of the signal (image). The $l1$-norm was optimized using a primal-dual algorithm, while the TV optimization was performed with both log barrier and the Newton iterative algorithms [33]. Fig. 4(a) shows an image of three fluorescent microspheres with full measurement (CR=1). We evaluated recovered image quality using a peak signal to noise ratio (PSNR), which is defined as [11,34],

$$PSNR = 10\log_{10}\left(\frac{|\max(X)|^2}{MSE(X^{CS})}\right)$$

where X^{CS} represents the compressed image, $\max(X)$, is the peak brightness of the uncompressed image that is reconstructed by full measurement, and $MSE(X^{CS}) = \frac{1}{N}\sum_i^N \left(X_i^{CS} - X_i\right)^2$ is the mean square error of the reconstructed image as compared with the uncompressed image. Since the real ground truth is inaccessible, the full sampled image [Fig. 4(a)] approximates the ground truth. As CR increases, the PSNR for images retrieved from all the algorithms decreases [Fig. 4(b)]. The TV optimization performs better than $l1$-norm with primal-dual optimization. Here, we show representative images for different compressed ratio under TV optimization with certain barrier, and in the absence of random noise (Newton algorithm) [Fig. 4(c)]. The TV with certain barrier tolerates random noise, thus allows considerably good image with CR up to 5. However, the TV with Newton optimization allows a CR as high as 10 with good image quality [Fig. 4(c)]. We anticipate that the PSNR would be further improved by using higher power density, brighter fluorophores, or detectors with higher sensitivity. Nevertheless, the presented work demonstrates the concept of wide-field TPM with encrypted acquisition using single-pixel detection and compressed sensing.

In conclusion, we demonstrated a custom-built femtosecond laser source and the application in single-pixel TPM. Structured illumination selectively excites the two-photon fluorescence fulfilled by excitation with spatially tailored structures. The patterns were secured with a random sequence, which naturally inhibits the image artefact. In contrast, the PMT provides faster speed and allows integration over a certain period of time for smooth image. Furthermore, the developed wide-field TPM offers three advantages for the communication of the acquired image. First, the single-pixel detection allows smaller data size as long as the receiver knows the encoding basis. Second, the random sequence makes

the decipher more challenging, thus, the data transfer more secure. Third, the compressed sensing reduces the data size and the communication channels. The proposed single-pixel encryption not only applies in TPM, but also in general can be applied in biomedical imaging where privacy-protection is desirable, such as single-pixel ophthalmoscope [35].

Acknowledgments

Research Grants Council of the Hong Kong Special Administrative Region, China (HKU 17209018, E-HKU701/17, CityU T42-103/16-N, HKU C7047-16G, and HKU 17205215) and Natural Science Foundation of China (N_HKU712/16).

References

1 M. F. Duarte, M. A. Davenport, D. Takhar, J. N. Laska, T. Sun, K. F. Kelly, and R. G. Baraniuk, IEEE Signal Processing Magazine **25,** 83 (2008).
2 M. P. Edgar, G. M. Gibson, and M. J. Padgett, Nature Photonics **13,** 13 (2018).
3 J. J. Field, D. G. Winters, and R. A. Bartels, Optica **3,** 971 (2016).
4 N. Radwell, K. J. Mitchell, G. M. Gibson, M. P. Edgar, R. Bowman, and M. J. Padgett, Optica **1,** 285 (2014).
5 S. S. Welsh, M. P. Edgar, R. Bowman, P. Jonathan, B. Sun, and M. J. Padgett, Optics Express **21,** 23068 (2013).
6 M. P. Edgar, G. M. Gibson, R. W. Bowman, B. Sun, N. Radwell, K. J. Mitchell, S. S. Welsh, and M. J. Padgett, Sci. Rep. **5,** 10669 (2015).
7 A.-X. Zhang, Y.-H. He, L.-A. Wu, L.-M. Chen, and B.-B. Wang, Optica **5,** 374 (2018).
8 W. L. Chan, K. Charan, D. Takhar, K. F. Kelly, R. G. Baraniuk, and D. M. Mittleman, Applied Physics Letters **93,** 121105 (2008).
9 H. Shen, L. Gan, N. Newman, Y. Dong, C. Li, Y. Huang, and Y. C. Shen, Optics Letters **37,** 46 (2012).
10 K. Ota and Y. Hayasaki, Optics Letters **43,** 3682 (2018).
11 Y. Liu, J. Suo, Y. Zhang, and Q. Dai, Optics Express **26,** 32451 (2018).
12 B. Sun, M. P. Edgar, R. Bowman, L. E. Vittert, S. Welsh, A. Bowman, and M. J. Padgett, Science **340,** 844 (2013).
13 S. S. Welsh, M. P. Edgar, R. Bowman, B. Sun, and M. J. Padgett, Journal of Optics **17,** 025705 (2015).
14 S. Ota, R. Horisaki, Y. Kawamura, M. Ugawa, I. Sato, K. Hashimoto, R. Kamesawa, K. Setoyama, S. Yamaguchi, K. Fujiu, K. Waki, and H. Noji, Science **360,** 1246 (2018).

[15] R. Horisaki, H. Matsui, R. Egami, and J. Tanida, Applied Optics **56,** 1353 (2017).
[16] M. Tanha, R. Kheradmand, and S. Ahmadi-Kandjani, Applied Physics Letters **101,** 101108 (2012).
[17] W. R. Zipfel, R. M. Williams, and W. W. Webb, Nature Biotechnology **21,** 1369 (2003).
[18] M. Gu, X. Gan, A. Kisteman, and M. G. Xu, Applied Physics Letters **77,** 1551 (2000).
[19] W. Denk, J. H. Strickler, and W. W. Webb, Science **248,** 73 (1990).
[20] X.-J. Tan, C. Kong, Y.-X. Ren, C. S. W. Lai, K. K. Tsia, and K. K. Y. Wong, Optics Letters **44,** 391 (2019).
[21] C. Kong, C. Pilger, H. Hachmeister, X. Wei, T. H. Cheung, C. S. W. Lai, T. Huser, K. K. Tsia, and K. K. Y. Wong, Biomedical Optics Express **8,** 4921 (2017).
[22] J. J. Field, K. A. Wernsing, S. R. Domingue, A. M. Allende Motz, K. F. DeLuca, D. H. Levi, J. G. DeLuca, M. D. Young, J. A. Squier, and R. A. Bartels, Proceedings of the National Academy of Sciences **113,** 6605 (2016).
[23] K. Tamura, E. P. Ippen, H. A. Haus, and L. E. Nelson, Optics Letters **18,** 1080 (1993).
[24] O. G. Okhotnikov, L. Gomes, N. Xiang, T. Jouhti, and A. B. Grudinin, Optics Letters **28,** 1522 (2003).
[25] A. Chong, J. Buckley, W. Renninger, and F. Wise, Optics Express **14,** 10095 (2006).
[26] D. Strickland and G. Mourou, Optics Communications **56,** 219 (1985).
[27] O. Katz, Y. Bromberg, and Y. Silberberg, Applied Physics Letters **95,** 131110 (2009).
[28] Y.-X. Ren, J. Wu, Q. T. K. Lai, H. M. Lai, D. M. D. Siu, W. Wu, K. K. Y. Wong, and K. K. Tsia, Light: Science & Applications **9,** 8 (2020).
[29] P. Clemente, V. Durán, V. Torres-Company, E. Tajahuerce, and J. Lancis, Optics Letters **35,** 2391 (2010).
[30] C. Yang, C. Wang, J. Guan, C. Zhang, S. Guo, W. Gong, and F. Gao, Photonics Research **4,** 281 (2016).
[31] Y.-X. Ren, R.-D. Lu, and L. Gong, Annalen der Physik **527,** 447 (2015).
[32] A. M. Paniagua-Diaz, I. Starshynov, N. Fayard, A. Goetschy, R. Pierrat, R. Carminati, and J. Bertolotti, Optica **6,** 460 (2019).
[33] See the toolbox for l1-optimization, https://statweb.stanford.edu/~candes/l1magic/.
[34] A. Pastuszczak, B. Szczygieł, M. Mikołajczyk, and R. Kotyński, Applied Optics **55,** 5141 (2016).
[35] B. Lochocki, A. Gambín, S. Manzanera, E. Irles, E. Tajahuerce, J. Lancis, and P. Artal, Optica **3,** 1056 (2016).

Figure Captions

Fig. 1. (a) Layout of the high-power femtosecond fiber laser. (b) Layout of single-pixel TPM. (c) Illustration of the single pixel imaging with structured illumination. HW, half waveplate; SMF, single mode fiber; PBS, polarizing beam splitter; G, grating; M, mirror; L, lens. F, short pass filter; O, objective; S, sample; other acronyms are explained in the text.

Fig. 2. (a) The temporal pulse train shows a repetition rate of 80 MHz. (b) Optical spectrum is centered at 1019 nm with 3 nm FWHM. (c) The autocorrelation curve suggests a pulse width of 550 fs.

Fig. 3. (a) Generation of hybrid basis and the complementary illumination patterns. (b) The recorded signals with (top) positive and negative patterns, and (bottom) the differential signal. (c) Retrieved image from (b) for 5 microspheres. (d) The eavesdropping image reconstructed with Hadamard basis using the same signal shown in (b). (e) The bright-field image of the same cluster of microspheres. (f~h) Single-pixel TPM images showing the robustness of the random sequenced Hadamard basis. Scale bar, 20 μm.

Fig. 4. (a) Uncompressed image. (b) PSNR as a function of the compression ratio for $l1$-norm with primal-dual algorithm (blue square), and total variance with log barrier (red star), and with Newton optimization (magenta circle). (c) Representative reconstructed images as function of compressing ratios for total variance optimization with (top) Newton and (bottom) log barrier algorithms.

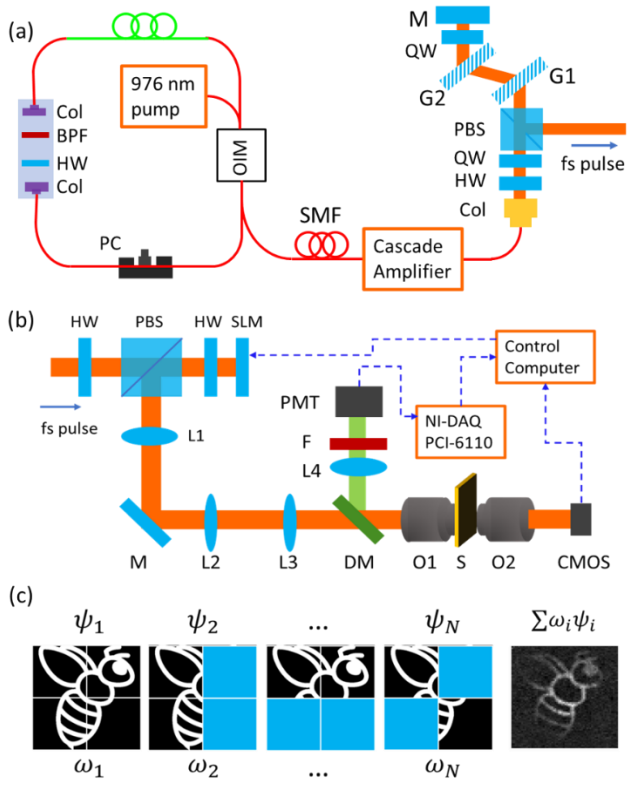

Fig.1.

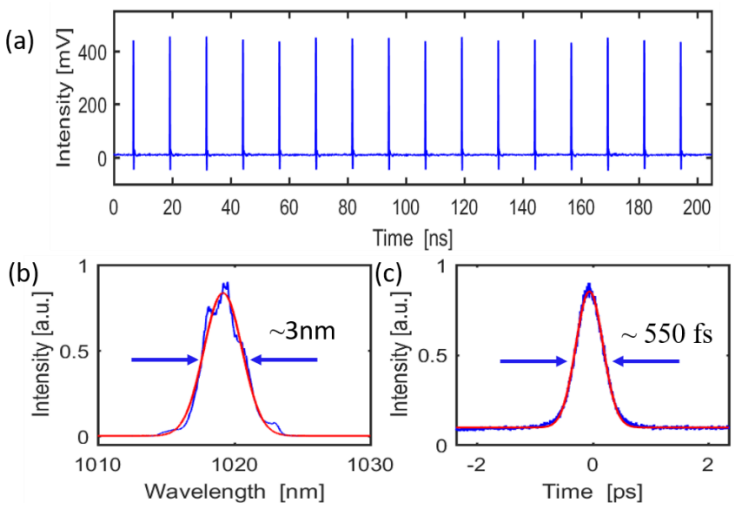

Fig. 2.

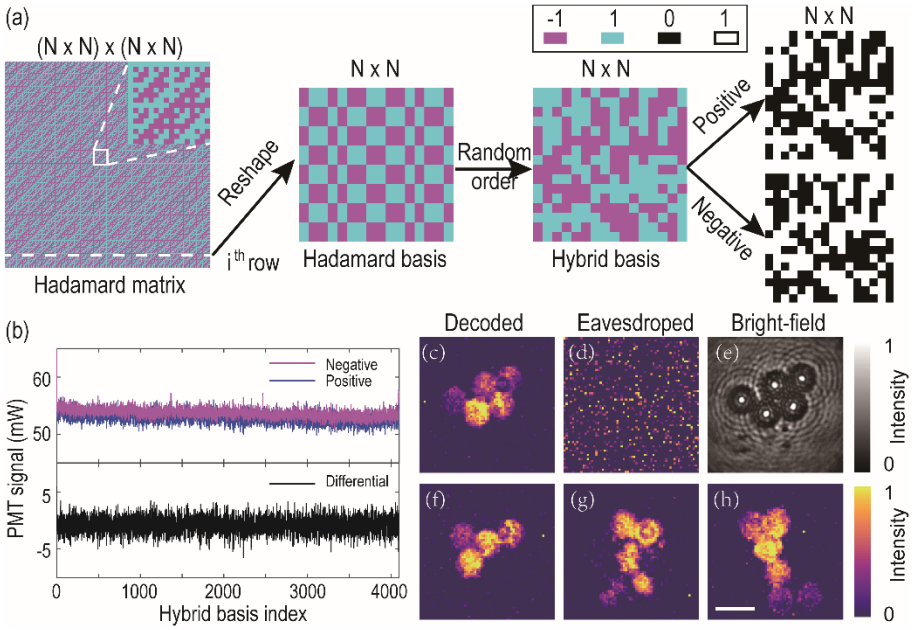

Fig. 3

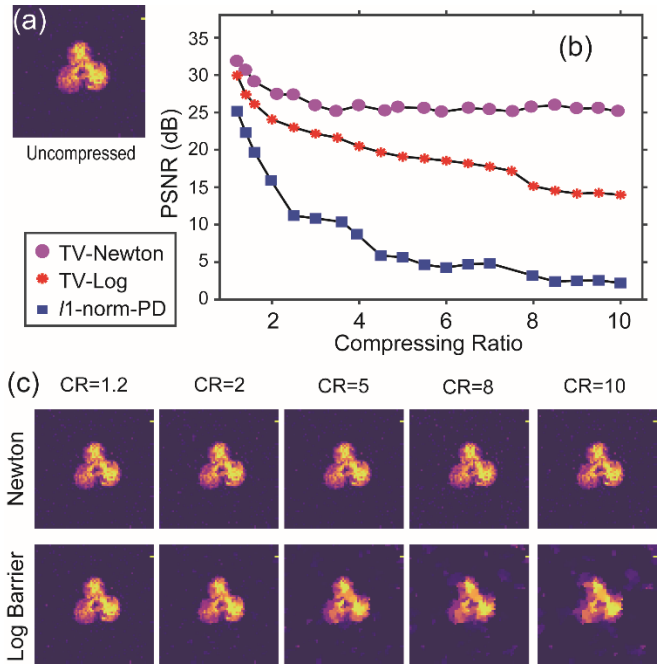
(a)
Uncompressed
(b)
PSNR (dB)
Compressing Ratio
TV-Newton
TV-Log
/1-norm-PD
(c)
CR=1.2
CR=2
CR=5
CR=8
CR=10
Newton
Log Barrier

Fig. 4